

Article

Engineering Porphyrin Metal–Organic Framework Composites as Multifunctional Platforms for CO₂ Adsorption and Activation

Jiewei Liu, Yan-Zhong Fan, Kun Zhang, Li Zhang, and Cheng-Yong Su

J. Am. Chem. Soc., **Just Accepted Manuscript** • DOI: 10.1021/jacs.0c05909 • Publication Date (Web): 25 Jul 2020

Downloaded from pubs.acs.org on July 25, 2020

Just Accepted

“Just Accepted” manuscripts have been peer-reviewed and accepted for publication. They are posted online prior to technical editing, formatting for publication and author proofing. The American Chemical Society provides “Just Accepted” as a service to the research community to expedite the dissemination of scientific material as soon as possible after acceptance. “Just Accepted” manuscripts appear in full in PDF format accompanied by an HTML abstract. “Just Accepted” manuscripts have been fully peer reviewed, but should not be considered the official version of record. They are citable by the Digital Object Identifier (DOI®). “Just Accepted” is an optional service offered to authors. Therefore, the “Just Accepted” Web site may not include all articles that will be published in the journal. After a manuscript is technically edited and formatted, it will be removed from the “Just Accepted” Web site and published as an ASAP article. Note that technical editing may introduce minor changes to the manuscript text and/or graphics which could affect content, and all legal disclaimers and ethical guidelines that apply to the journal pertain. ACS cannot be held responsible for errors or consequences arising from the use of information contained in these “Just Accepted” manuscripts.

Engineering Porphyrin Metal–Organic Framework Composites as Multifunctional Platforms for CO₂ Adsorption and Activation

Jiwei Liu^{a,b,d}, Yan-Zhong Fan^{+c}, Kun Zhang^a, Li Zhang^{*c}, Cheng-Yong Su^{*c}

^aSchool of Biotechnology and Health Sciences, Wuyi University, Jiangmen 529020, P.R. China.

^bInternational Healthcare Innovation Institute (Jiangmen), Jiangmen 529040, P. R. China.

^cMOE Laboratory of Bioinorganic and Synthetic Chemistry, Lehn Institute of Functional Materials, School of Chemistry, Sun Yat-Sen University, Guangzhou 510275, China.

^dSchool of Chemical Engineering and Light Industry, Guangdong University of Technology, Guangzhou 510006, P. R. China

ABSTRACT: As an effective solution towards the establishment of a sustainable society, the reductive transformation of CO₂ into value-added products is certainly important and imperative. Herein, we report that a porphyrin metal-organic framework composite Au@Ir-PCN-222, which is obtained through the *in situ* formation of Au nanoparticles in the coordination interspaces of Ir-PCN-222. Catalytic results show that Au@Ir-PCN-222 is highly efficient for CO₂ reduction and aminolysis, giving rise to formamides in high yields and selectivities under room temperature and atmospheric pressure. Mechanistic studies disclose that the high efficiency of Au@Ir-PCN-222 is due to the synergistic catalysis of Au NPs and Ir-PCN-222, in which Au NPs can adsorb CO₂ molecules on their surfaces and then increase the CO₂ concentration in the cavities of the framework, and at the same time, Au NPs transfer electrons to Ir-porphyrin units and therefore increase the interactions with CO₂ molecules.

1. INTRODUCTION

With the continuous consumption of fossil energy by human activities, the emission of the greenhouse gas carbon dioxide (CO₂) caused a series of environmental problems such as global warming and the acidification of oceans. The report of the International Energy Agency suggested that the average concentration of CO₂ was 400 ppm in 2018, and predicted that CO₂ concentration might reach 950 ppm by 2100.¹ As an effective solution towards the establishment of a sustainable society, the reductive transformation of CO₂ into value-added products is certainly important and imperative.²⁻⁴ Among the CO₂ reduction reactions, the synthesis of formic acid by hydrogenation of CO₂ with hydrogen (H₂) has attracted much interests, but this is a thermodynamically unfavourable reaction ($\Delta G = +33 \text{ kJ}\cdot\text{mol}^{-1}$) and requires high CO₂ and H₂ pressures and elevated temperatures.⁵ In contrast, CO₂ reduction in the presence of silanes as the reductants, which is also termed as CO₂ hydrosilylation, is a thermodynamically favored chemical process ($\Delta G = -29.3 \text{ kJ}\cdot\text{mol}^{-1}$), due to the cleavage of weaker Si–H bonds and the formation of stronger Si–O bonds.⁶ Remarkably, silyl formates, which are formed from CO₂ hydrosilylation, are of great interest due to their potential application as synthons for the preparation of a wide range of valuable chemicals such as formic acid, formamides and formates with the addition of water, amines and alcohols, respectively.⁷

A few homogeneous reaction systems using transition metal complexes⁸⁻¹³ or organocatalysts¹⁴⁻¹⁷ have been reported for CO₂ hydrosilylation under mild conditions (RT and 1 atm) and with high selectivities. As an emerging class of porous materials, metal-organic frameworks (MOFs) are promising heterogeneous candidates, although their catalytic

performances towards CO₂ hydrosilylation are rarely studied yet.^{18,19} The plentiful reticular chemistry of MOF structures offers opportunities for the rational design of MOF composites, which integrate CO₂ adsorption and activation.²⁰⁻²² Firstly, the non-bonded interactions between CO₂ and the open metal sites or heteroatoms in the catalytic coordination spaces of MOFs help increase the local CO₂ coverage nearby the active sites.²³ The cavities of MOFs can be further used for the immobilization of co-catalysts, especially metal nanoparticles (MNPs), which can adsorb CO₂ molecules (Figure S1).^{24,25} Secondly, the homogeneous catalysts as the ligands can be incorporated into the frameworks and dispersed uniformly within the MOFs, giving rise to heterogeneous single-site catalysts.^{26,27} Moreover, the charge-transfer interaction between the electron-rich MNPs and MOFs becomes a critical factor for controlling the catalytic reactivity of the resultant M@MOF composites,²⁸⁻³¹ which could increase the electron density of the MOF, and thereafter enhance its interactions with CO₂ via the back bonding, that is, the electron transfers from the occupied d orbitals of the metal to the LUMO of CO₂.^{32,33} Thirdly, the definite and uniform structures of MOFs will benefit the study of the interactions between CO₂ and frameworks at a molecular level, which is critical for the design of more powerful catalysts.³⁴⁻³⁶

In this paper, we report the preparation of a series of porphyrin metal-organic frameworks M-PCN-222 (which are also denoted as M-PMOF-2) through the self-assembly of ZrCl₄ and M-TCPP (M = Ru, Rh, Pd, Ir, Pt; TCPP = tetrakis(4-carboxyphenyl)porphyrin)).³⁷⁻⁴¹ The MOFs possess a *csq* topology as in PCN-222⁴², MOF-545⁴³ or MMPF-6⁴⁴, and contain hexagonal and triangular channels with the diameters of 3.7 and 1.3 nm, respectively. The micro cavities are used for CO₂ reservoirs whereas the meso cavities are used for the immobilization of metal nanoparticles (MNPs) such as Pd, Ir, Pt and Au.⁴⁵⁻⁴⁷ The resultant M@M-PCN-222 can be

functionalized as a multifunctional platform, integrating CO₂ adsorption and activation. Catalytic results and mechanistic studies show that, due to the synergistic catalysis of Au NPs and Ir-PCN-222, in which Au NPs can adsorb CO₂ molecules on their surfaces and then increase the CO₂ concentration in the cavities of the framework, and at the same time, Au NPs transfer electrons to Ir-porphyrin units and therefore increase the interactions with CO₂ molecules, Au@Ir-PCN-222 is highly efficient for CO₂ reduction and aminolysis, giving rise to formamides in excellent yields and selectivities under room temperature and atmospheric pressure (Figure 1).

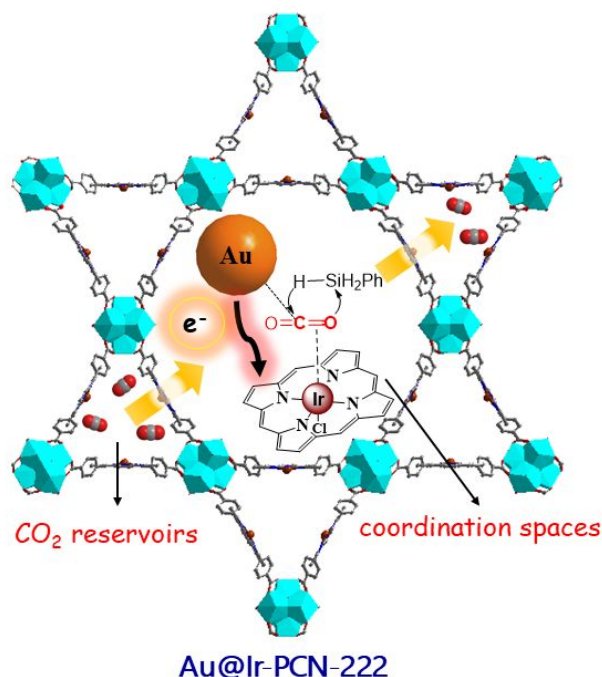


Figure 1. CO₂ adsorption, diffusion and activation in the inner cavities of Au@Ir-PCN-222.

2. EXPERIMENTAL SECTION

2.1 Synthesis of Ir-PCN-222

After a mixture of Ir(TCPP)Cl (10 mg, 0.01 mmol), ZrOCl₂·8H₂O (20 mg, 0.06 mmol), trifluoroacetic acid (300 μL) and H₂O (100 μL) in *N,N*-dimethylformamide (2 mL) is heated at 130 °C for 6 h, red needle-like crystals (10.9 mg, 60% yield) are obtained and dried under vacuum at 120 °C overnight for further characterizations and uses. Anal. Calcd. for C₄₈H₃₂IrClN₄O₁₆Zr₃·3DMF·10H₂O (C₅₇H₇₃IrClN₇O₂₉Zr₃): C, 37.58; H, 3.04; N, 5.38%. Found: C, 37.12; H, 3.74; N, 5.82%. FT-IR (KBr) ν 3257 (br), 2858 (br), 1587 (s), 1541 (s), 1371 (s), 1067 (s), 1010 (s), 906 (m) cm⁻¹.

2.2 Synthesis of Au@Ir-PCN-222

The suspension of the activated Ir-PCN-222 sample (20 mg) in dry *n*-hexane (5 mL) is sonicated for around 5 min until it becomes homogeneous. And then, the HAuCl₄ aqueous solution (20 mg·mL⁻¹, 100 μL) is added dropwise with constant vigorous stirring. The resultant solution is stirred for 2 h, and then the reaction mixture is centrifuged to remove the supernatant. To the harvested sample is added ascorbic acid solution (6 mg·mL⁻¹, 5 mL). After being stirred for 2 h, the product is separated as

red needle-like crystals via centrifugation at 12000 rpm for 2 min, washed with ethanol for several times, and dried under vacuum at 120 °C overnight.

2.3 Catalytic reaction

Typically, a mixture of phenylsilane (PhSiH₃, 216 mg, 2 mmol), *N*-methylaniline (**1a**, 107.0 mg, 1 mmol), cesium carbonate (Cs₂CO₃, 6.5 mg, 0.02 mmol) and activated Au@Ir-PCN-222 (10 mg, 0.008 mmol) is stirred in THF (2 mL) under atmospheric CO₂ at room temperature. After 2 h, the reaction mixture is centrifuged. The recycled catalyst is washed with DCM (5 mL × 4), dried in the air and reused in the consecutive runs. The combined supernatant is evaporated to dryness, which is purified by flash chromatography to afford the pure product *N*-methyl-*N*-phenylformamide (**2a**, 117 mg, 87% yield). ¹H NMR (400 MHz, CDCl₃) of **2a**: δ 8.44 (s, 1H), 7.37 (m, 2H), 7.24 (m, 1H), 7.15 (m, 2H), 3.28 (s, 3H).

2.4 Computational details

2.4.1 The molecular model of Ir-PCN-222

The periodic crystal structure of Ir-PCN-222 for calculation is based on the reported Fe-PCN-222⁴² and is relaxed by geometry optimization on the package of CP2K 2.6.1.⁴⁸ The calculation employs the Perdew-Burke-Ernzerhof functional (GGA-PBE)⁴⁹ while the Kohn-Sham orbitals for all atoms are expanded into an atom-centered double- ζ quality DZVP-MOLOPT-GTH Gaussian basis set.⁵⁰ The pseudopotentials used for all of the atoms are those derived by Goedecker, Teter and Hutter.⁵¹ The cutoff energy of 650 Ry and the cutoff in reciprocal space of 80 are considered, respectively.

Based on the crystal structure of Ir-PCN-222, the molecular models of Ir(TMCP)Cl (TMCP = 5,10,15,20-tetrakis(4-methoxycarbonylphenyl)porphyrin) and Zr₆O₈ clusters are further calculated by the package of Gaussian 09.⁵² By ChelpG method,⁵³ Minnesota functional M06L⁵⁴ that can perform quite well in transit-metal system is applied to fit their electrostatic potential (ESP) charges with a hybrid basis set of split valence 6-311G**⁵⁵ for C, H, N and O while Stuttgart and Dresden (SDD) pseudopotentials⁵⁶ for Ir, Zr and Cl. In these calculations, the atomic van der Waals radii for all atoms of the Ir-PCN-222, which are used to fit the ESP charges, are taken from the work of Batsanov.⁵⁷

2.4.2 The surface model of Au@Ir-PCN-222

After cleaving the (100) plane of crystal, a vacuum slab of 20 Å is stacked to build the surface model. Based on Garzón's work, one Au₃₈ nanocluster that is confirmed as one of the lowest energy structures, is created near the coordinated water molecules of Zr₆O₈ clusters.⁵⁸ All the calculation for density of states (DOS) is carried on the package of CP2K 2.6.1 at the near level for geometry optimization.⁴⁸ To describe the function of Au₃₈ nanocluster in CO₂ activation, the revised PBE functional (revPBE), which is constructed by optimizing parameters of PBE against the exchange energy, is used to compute the surface model without nanocluster to illustrate the impact between adatoms and channel-wall atoms for comparison.⁵⁹

2.4.3 CO₂ adsorption sites of Ir-PCN-222

The interactions between the Ir-PCN-222 frameworks and the CO₂ were modelled using the sum of a 12-6 Lennard-Jones (LJ) contribution and a Coulombic term. The Universal Force Field (UFF)⁶⁰ and DREIDING⁶¹ force fields are adopted to describe the LJ parameters for the atom of the inorganic nodes

and organic linkers of the MOFs respectively. In this work, the parameters of CO₂ molecule are described by Elementary physical model 2 (EPM2).⁶²

A 1×1×2 supercell for Ir-PCN-222 is considered with cell parameters that exceed 24 Å in order to be able to apply a cutoff radius of 12 Å for the short-range dispersion. The long-range electrostatic interactions are handled using the Ewald summation technique. The fugacities for CO₂ at a given thermodynamic condition are computed with the Peng-Robinson equation of state (EoS).⁶³ The Grand Canonical Monte Carlo (GCMC) simulations are performed using the Complex Adsorption and Diffusion Simulation Suite (CADSS) code.⁶⁴ For each fugacity point, the system is sustained under 2×10⁸ equilibrium steps and 1×10⁸ product steps under a constant temperature 273 K. The configuration of adsorbate is calculated through GCMC simulations using the revised Widom's test particle insertion method.⁶⁵

2.4.4 CO₂ diffusion in Ir-PCN-222

Molecular dynamics (MD) simulations are carried out by LAMMPS package⁶⁶ to illustrate the transport diffusivity of CO₂ in Ir-PCN-222. The structure with saturated adsorption is obtained from the snapshot of the GCMC simulation. Considering that total energy of the system keeps constant in the process of diffusion, the simulation is performed in microcanonical ensemble (NVE) at 273.15 K with the timestep as 1 fs. For fluid simulation, Langevin equation^{67,68} is used to control the kinetic energy of rigid bodies system, of which the temperature is relaxed in 1 ps. The structure optimized with forcefield is first equilibrated with the time of 10 ns, followed by 50 ns production MD. The same parameters and cutoff radius of van der Waals and long-range Coulombic potential from GCMC simulation are employed to represent non-bonded interaction. Considering the rigidity of Ir-PCN-222, only the movements of CO₂ are taken into consideration to simulate the process of diffusion. The bonded forcefield parameters for CO₂ are consulted from Myshakin's work.⁶⁹

The self-diffusivity D_s is obtained from mean squared displacement (MSD) by Einstein equation,⁷⁰

$$D_s = \frac{1}{2dN} \lim_{t \rightarrow \infty} \frac{d}{dt} \left\langle \sum_{i=1}^N |r_i(t) - r_i(0)|^2 \right\rangle$$

where $r_i(t)$ denotes as position of the adsorbate molecule i at time t , d and N represents the dimension of the system and the number of diffusing molecules in the system under ensemble average.

2.4.5 Reaction kinetics of CO₂ hydrosilylation

The transit state search is carried on Gaussian 09⁵² package with the same functional mentioned previously. Split valence basis set 6-311G**⁵⁵ is employed to describe C, H, N and O, while Def2SVP for Ir, Cl, Au and Si.^{71,72}

3. RESULTS AND DISCUSSION

3.1 Syntheses and characterizations

Ir-PCN-222 is prepared through the assembly of ZrCl₄ and Ir(TCPP)Cl in the presence of trifluoroacetic acid as a modulating reagent at 130 °C for 6 h. Powder X-ray diffraction (PXRD) patterns confirm the bulk purity of the as-prepared samples (Figure S2), which fit well with the simulated patterns of PCN-222 that is constructed with metal free porphyrin ligand

TCPP.⁴² The morphology of Ir-PCN-222 is revealed by scanning electron microscopy (SEM) and transmission electron microscopy (TEM), indicating that the as-prepared Ir-PCN-222 samples are in three-dimensional, rod-shaped structures with about 600 nm width and 3 μm length (Figure 2a and 2b).

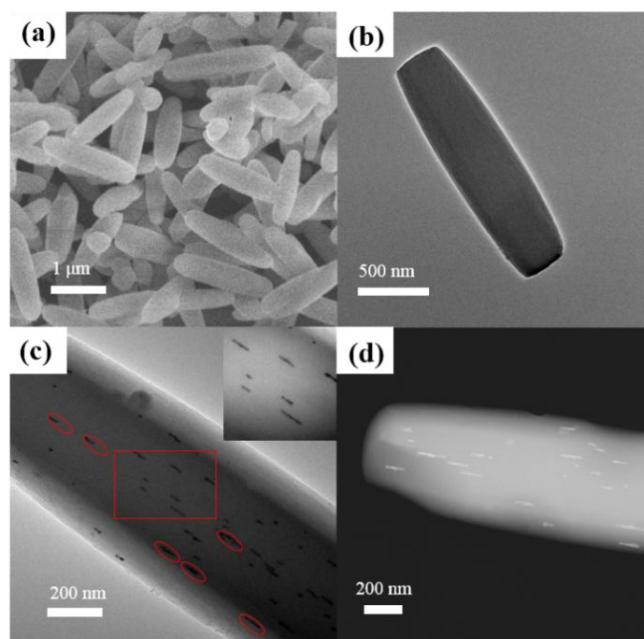


Figure 2. SEM (a) and TEM (b) images of Ir-PCN-222, and median-magnification TEM (c), high-magnification TEM (insert c) and aberration-corrected HAADF-STEM (d) images of Au@Ir-PCN-222.

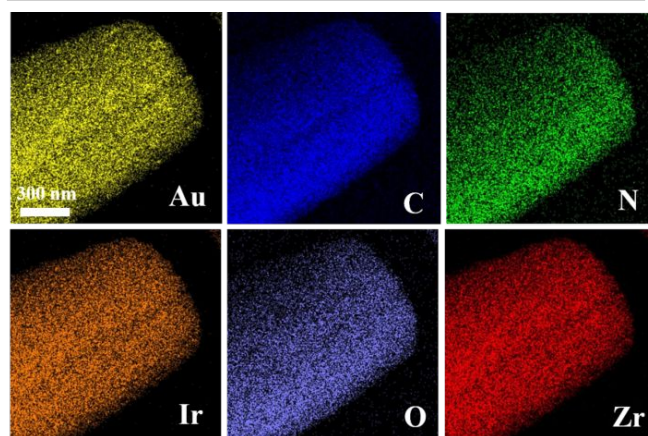


Figure 3. TEM-EDX elemental mapping images of Au@Ir-PCN-222 corresponding to Au, C, N, Ir, O and Zr elements, respectively.

The MOF composite Au@Ir-PCN-222 is prepared by the *in situ* formation of Au NPs in Ir-PCN-222, which is achieved by using a double-solvent approach (DSA). The PXRD pattern of Au@Ir-PCN-222 is well matched with that of the pristine Ir-PCN-222, indicating that the framework and crystallinity of Ir-PCN-222 remain well after the introduction of Au NPs (Figure S2). The presence of Au NPs in Au@Ir-PCN-222 is clearly observed in the TEM images, which is marked with the red circles in Figure 2c and the inset. The Au NPs with a width of around 3 nm display consistent orientation (Figure 2d), indicative of the confined growth of Au NPs starting from the

single crystal, nanocube to nanobar with a length range of 20–60 nm in the hexagonal mesochannels (Figures S3 and S4).⁷³ The existence of the consistent orientation growth of Au NPs in Ir-PCN-222 is also evidenced by the high-angle annular dark-field scanning TEM (HAADF-STEM) tomogram analysis (Figure 2d). Meanwhile, the TEM-EDX (energy dispersive X-ray spectroscopy) elemental mapping images demonstrate the uniform distribution of all of the elements in the whole Au@Ir-PCN-222 (Figure 3). The weight loading of Au NPs is determined to be 2% using an inductively coupled plasma mass spectrometry (ICP-MS).

The permanent porosity of Ir-PCN-222 and Au@Ir-PCN-222 has been confirmed by N₂ adsorption isotherms at 77 K, and the Brunauer-Emmett-Teller (BET) surface areas are calculated to be 2387 and 1452 m²·g⁻¹, respectively (Figure S5). The pore size distribution of Ir-PCN-222 that is calculated using the density function theory (DFT) simulation discloses that there are two types of pores, with the sizes of 1.2 and 3.4 nm, respectively (Figure S6), which is well matched to the crystal structure of PCN-222 when van der Waals interaction is considered.

X-ray photoelectron spectroscopy (XPS) examination is used to confirm the existence and oxidation state of Ir in Ir-PCN-222 (Figure S7). The +3 valance state of Ir is clearly evidenced by the binding energies at 62.6 and 65.6 eV, assignable to the 4f_{7/2} and 4f_{5/2} levels of Ir(III), respectively. After the incorporation of Au NPs into the pores of Ir-PCN-222, the Au XPS spectrum of resultant composites presents two peaks with binding energies of 84.3 and 87.8 eV, corresponding to Au⁰ 4f_{7/2} and Au⁰ 4f_{5/2}, respectively (Figure S8). It is noted that Ir 4f binding energies of Au@Ir-PCN-222 (4f_{7/2}, 62.4 eV and 4f_{5/2}, 65.3 eV) are slightly shifted toward lower oxidation states than those of Ir-PCN-222, suggesting that the charge-transfer interactions exist between Au NPs and Ir-PCN-222 (Figure S9).^{28–31}

The calculations for density of states (DOS) have been carried out on the package of CP2K 2.6.1 at the near level for geometry optimization.⁴⁸ Based on Garzón's work, one Au₃₈ nanocluster that is confirmed as one of the lowest energy structures, is created near the coordinated water molecules of Zr₆O₈ clusters (Figure S10).⁵⁸ The O partial DOS of surface model with/without Au₃₈ nanocluster are shown in Figure S11. As a metal cluster, the inclusion of the guest Au₃₈ increases Fermi energy by 0.40 eV and metallizes the host Ir-PCN-222, which is consistent with the XPS experimental analysis.

3.2 CO₂ adsorption and diffusion

The adsorption behaviors of Ir-PCN-222 and Au@Ir-PCN-222 towards CO₂ are evaluated (Figure 4 and Table S1). The CO₂ adsorption isotherms at different temperatures (e.g. 298 and 308 K) are carried out and disclose that both Ir-PCN-222 and Au@Ir-PCN-222 show high adsorption capability of CO₂ at 1 bar, whereas Au@Ir-PCN-222 displays higher adsorption performances due to the adsorption of CO₂ on the surfaces of Au NPs.²⁵ The isosteric heats of adsorption (Q_{st}) are calculated from the CO₂ sorption data by the virial fitting method (Figures S12–15).⁷⁴ The initial Q_{st} of Ir-PCN-222 and Au@Ir-PCN-222 are up to 26.9 and 29.0 kJ·mol⁻¹, respectively, indicative of specific CO₂ adsorption sites embedded in the pore walls. The higher initial Q_{st} value of Au@Ir-PCN-222 than Ir-PCN-222 further shows that, with the incorporation of Au NPs into the inner cavities of Ir-PCN-222, the resultant composite Au@Ir-PCN-222 shows stronger interaction with the CO₂ molecules.

The snapshot of CO₂ adsorbed in Ir-PCN-222 is obtained from the results of the Grand Canonical Monte Carlo (GCMC)

simulation (Figure 5 and Table S2). The results unveil that, in the mesopores, the potential CO₂ adsorption sites are mainly near the coordinated water of Zr₆O₈ clusters (site 1), and some others lay behind the Ir-Cl paralleled with porphyrin. As for site 1, the electrostatic potential (ESP) charge of the Zr element is +1.9930 |e| (Figure S16), which might interact with the nucleophilic O atoms in CO₂, but the van der Waals interactions from the coordinated water keep a distance between Zr₆O₈ clusters and free CO₂ molecules. On the other hand, in the micropores, CO₂ molecules mainly interact through their ESP charges on C atoms with the axial Cl atoms (d_{C-Cl} = 3.2–3.3 Å, site 2). Radial distribution function (RDF) is further applied to investigate the specific distance in cavity (Figure S17), and the results show that site 1 and site 2 are validated in the peaks of O(H₂O)-CO₂ (d_{C-O} = 3.8 Å) and Ir-CO₂ (d_{C-Cl} = 3.5 Å), respectively.

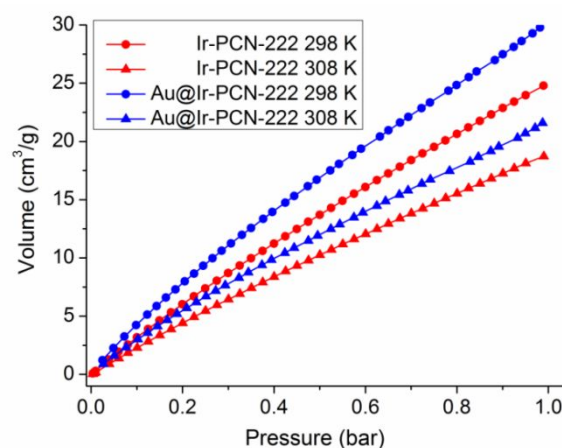


Figure 4. The CO₂ adsorption-desorption isotherms of Ir-PCN-222 and Au@Ir-PCN-222.

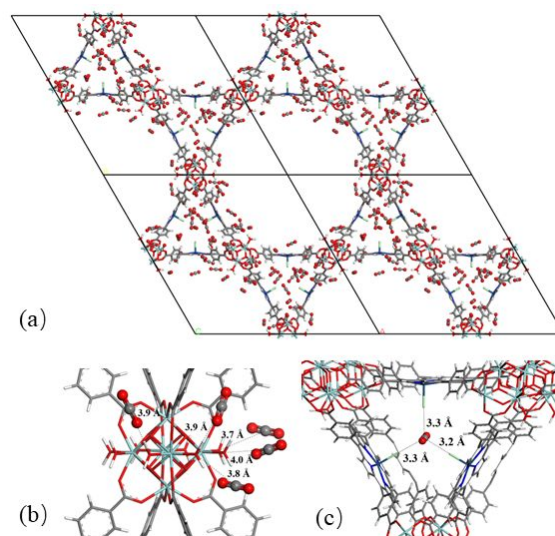


Figure 5. Snapshot of CO₂ molecules adsorbed in Ir-PCN-222 from the simulation (a) and the preferred CO₂ adsorption site 1 (b) and site 2 (c) from GCMC simulation. The specific conformations in the snapshot are marked with the distance.

These experimental and simulation results disclose the CO₂-framework interactions, the potentials of the inner cavities of Ir-PCN-222 as CO₂ reservoirs, and the possible active sites for CO₂ activation. Based on these results, it may be concluded that the trigonal channels are favorable for CO₂ adsorption and meanwhile the hexagonal channels become the platform for CO₂ activation. To testify this hypothesis, the potential barriers are calculated by displacing a single molecule of CO₂ along the direction from micropore to mesopore between the neighboring porphyrin structures (Figure 6). It can be concluded from the results that the diffusion process from two scales of pores is reversible with 5 kJ·mol⁻¹ as potential barriers.

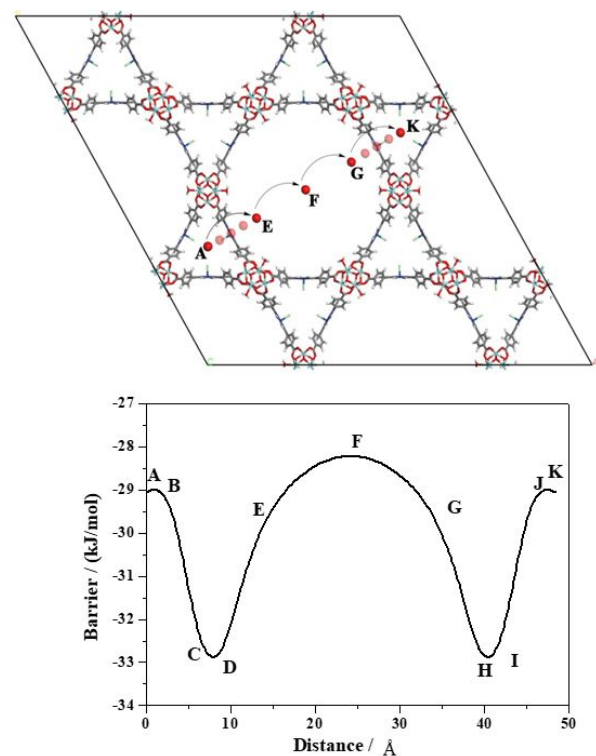


Figure 6. Potential energy distributions for one CO₂ molecule along the direction of micropore – mesopore – micropore.

To illustrate the possibility from a more direct parameter, molecular dynamics (MD) simulations are carried out to illustrate the transport diffusivity of CO₂ in Ir-PCN-222. Based on the trajectories recorded during MD runs, the average residence times inside the mesopores (t_{meso}) and micropores (t_{micro}) are calculated to be 18.22 and 20.00 ns, respectively. When the CO₂ molecules in the mesopores are exhausted with the reaction going on, the interchange of adsorbate between two scales of pores could occur due to a dynamic state of equilibrium. Meanwhile, the CO₂ diffusion process from micropores to mesopores is recorded in the movie (Supporting Information), which can vividly display CO₂ transportation in Ir-PCN-222. In order to illustrate the influence of CO₂ concentration on diffusion, the diffusivities at different loading are obtained from four trajectories (Figure S18). The diffusivities (3.6×10^{-11} m²/s) of CO₂ in Ir-PCN-222 (38 CO₂ per unit cell) are rather lower compared to other MOFs,^{75,76} indicative of the relatively strong non-bonded interactions between CO₂ molecules and Ir-PCN-222 (Table S3). The decreased speed of CO₂ transferring from micropores to

mesopores is consistent with the goal to use micropores as CO₂ reservoirs, which is beneficial for catalytic reactions to be carried out in the mesopores of Ir-PCN-222.

3.3 Catalysis and reaction mechanism

The catalytic performances of PMOFs and PMOF composites towards CO₂ reduction and aminolysis are studied under atmospheric pressure and ambient temperature (Table 1). Ir-PCN-222 is efficient for the reaction, giving rise to formamide (**2a**, C^{+II} species) and *N,N*-dimethylaniline (**3a**, C^{-II} species) in the yield of 89% and a selectivity of 98:2 (entry 1). For comparison, the PMOFs based on the other two d⁶ metal porphyrins such as Rh-PCN-222 and Ru-PCN-222 display much poorer performances and give rise to low to modest yields (entries 2 and 3). Neither Pd-PCN-222 nor Pt-PCN-222 can promote the reaction (entries 4 and 5). Controlled experiments further show that PCN-222 with no metal in the porphyrin can't work at all (entry 6). There isn't any background reaction in the absence of any catalyst (entry 7). It is clear that the incorporation of Ir into the porphyrin macrocycle plays an important role on the catalytic performances of PMOFs.

Table 1. Catalyst screening.^a

Entry	Catalyst	Reaction Time (h)	Yield (%) ^b	Molar ratio (2a:3a)	TON	TOF (h ⁻¹)
1	Ir-PCN-222	24	89	98:2	109	4.5
2	Rh-PCN-222	24	42	98:2	51	2.1
3	Ru-PCN-222	24	11	87:13	12	0.5
4	Pd-PCN-222	24	0	/	/	/
5	Pt-PCN-222	24	0	/	/	/
6	PCN-222	24	0	/	/	/
7	none	24	0	/	/	/
8	Ir@Ir-PCN-222	2	81	93:7	94	47
9	Pd@Ir-PCN-222	2	79	87:13	86	43
10	Pt@Ir-PCN-222	2	75	67:33	63	31.5
11	Au@Ir-PCN-222	2	90	91:9	102	51.1
12	Au NPs	24	0	/	/	/
13	Ir-PCN-222 + Au NPs	2	47	92:8	54	27

^aReaction condition: CO₂ (1 atm), *N*-methylaniline (**1a**, 1 mmol, 107 mg), PhSiH₃ (2 mmol, 216 mg), catalyst (0.8 mol%), Cs₂CO₃ (0.018 mmol, 6 mg), THF (2 mL), 60 °C, 24 h. ^bThe yield is the conversion of **1a** to **2a** and **3a**, which is determined by ¹H NMR using 1,3,5-trimethoxybenzene as an internal standard.

To our delight, after the immobilization of noble metal NPs into the hexagonal mesochannels of Ir-PCN-222, the resultant PMOF composites M'@Ir-PCN-222 (M' = Ir, Pd, Pt, Au) display enhanced catalytic efficiencies (entries 8-11). Among them, Au@Ir-PCN-222 is the most efficient. M'NPs in the M'@Ir-PCN-222 composites can adsorb CO₂ molecules on their surfaces and then increase the CO₂ concentration in the cavities

of the framework. At the same time, M'NPs transfer electrons to Ir-porphyrin units and therefore increase the interactions with CO₂ molecules. As for the electron transfer from M'NPs to Ir-PCN-222, there is difference among different M'NPs due to the orbital occupation.⁷⁷ The stable electron structures of an atom are those with its atomic orbital fully filled (d¹⁰), half-filled (d⁵), or empty (d⁰). Ir-PCN-222 is difficult to obtain electrons from Pd⁰ (4d¹⁰) or Pt⁰ (5d¹⁰) NPs because these metals are stable with their fully filled electron states. Besides, Ir⁰ (5d⁹) is inclined to obtain an electron to form 5d¹⁰ while reluctant to donate it any more. By contrast, Au⁰ (5d¹⁰6s¹) is ready to donate one electron to form 5d¹⁰, which might explain Au@Ir-PCN-222 displays the highest reaction efficiency among M'@Ir-PCN-222 composites (M' = Ir, Pd, Pt, Au).

To explore the effect of Au NPs, the polyvinyl pyrrolidone (PVP) stabilized Au NPs are prepared and applied in the same reaction. It is found that no reaction occurs at all when Au NPs are used as the sole catalyst (entry 12). The results disclose that Ir-PCN-222 instead of Au NPs is the catalytically active sites within Au@Ir-PCN-222, but nevertheless, the synergistic catalysis of these two components largely increases the reaction efficiency. In addition, the simple mixture of Au NPs and Ir-PCN-222 can only induce a modest yield of 54% in 2 h (entry 13).

The substrate scope regarding to amines is studied using Ir-PCN-222 as the catalyst (Table 2). It is found that a series of *para*-substituted *N*-alkylanilines perform smoothly to give the corresponding formamides (**2a-e**) with the yield range of 77-87%. Indoline and 1,2,3,4-tetrahydroquinoline can react with CO₂ in the presence of PhSiH₃ as the reducing reagent, and the formamides **2f** and **2g** are produced in 95 and 75% yields, respectively. The primary amine aniline can be also involved in the catalytic reaction, producing *N*-phenylformamide (**2h**) in a high yield (85%). Dialkyl-substituted secondary amines display good to excellent yields to the corresponding products (**2i-l**) with the yields of 71%-90%.

Table 2. Substrate scope.^a

CO ₂ (1 bar)	PhSiH ₃	1 R ¹ R ² NH	Ir-PCN-222 (0.8 mol%) Cs ₂ CO ₃ THF, R. T.	R ¹ R ² 2 N-CHO
2a (87%)		2b (77%)		2d (78%)
2e (67%)		2f (95%)		2h (85%)
2i (90%)		2j (72%) ^b		2l (71%) ^b

^aReaction condition: CO₂ (1 atm), **1** (1 mmol), Ir-PCN-222 (0.8 mol%), PhSiH₃ (2 mmol, 216 mg), Cs₂CO₃ (0.018 mmol, 6 mg), THF (2 mL), R. T. for 24-48 h. The yields are isolated yield; ^bThe yield is the conversion of **1** to **2**, which is determined by ¹H NMR using 1,3,5-trimethoxybenzene as an internal standard.

Recycling experiments have been studied to show the robustness of Au@Ir-PCN-222 as a heterogeneous catalyst. The results show that no significant activity loss occurs during four successive runs (Figure S19). The TEM image of the recycled Au@Ir-PCN-222 indicates that it almost maintains its morphology (Figure S20). The PXRD of the recycled samples further confirm that the crystallinity of Au@Ir-PCN-222 remains intact after the catalytic reactions (Figures S21). The XPS spectrum of the recycled Au@Ir-PCN-222 sample after the catalytic reaction shows that the +3 valance state of Ir remains. As shown in Figure S22, the peaks with the binding energies at 62.4 and 65.3 eV are assignable to the 4f_{7/2} and 4f_{5/2} levels of Ir(III), respectively. ICP-MS analysis of the filtrate after catalysis discloses that the amount of Au leaching into the reaction mixture is around 0.21%.

The hydrosilylation of CO₂ might occur through either an outer-sphere or inner-sphere pathway (Figure 7).^{2,4} As for the outer sphere pathway, the CO₂ hydrosilylation process is initiated by phenylsilane coordination to the iridium center via a η²-(Si-H) mode, and ends with transfer of silyl and hydride ligands to CO₂ in a concerted way. For comparison, in the inner sphere pathway, the iridium center firstly interacts with the CO₂ molecule in the side-on (η²-C,O) coordination, and then the coordinated CO₂ reacts with phenylsilane in the similar concerted way as the outer sphere pathway. Both pathways lead to the formation of the silyl formate as the intermediate, which then react with amines (**1**) to generate the final products of formamides (**2**).

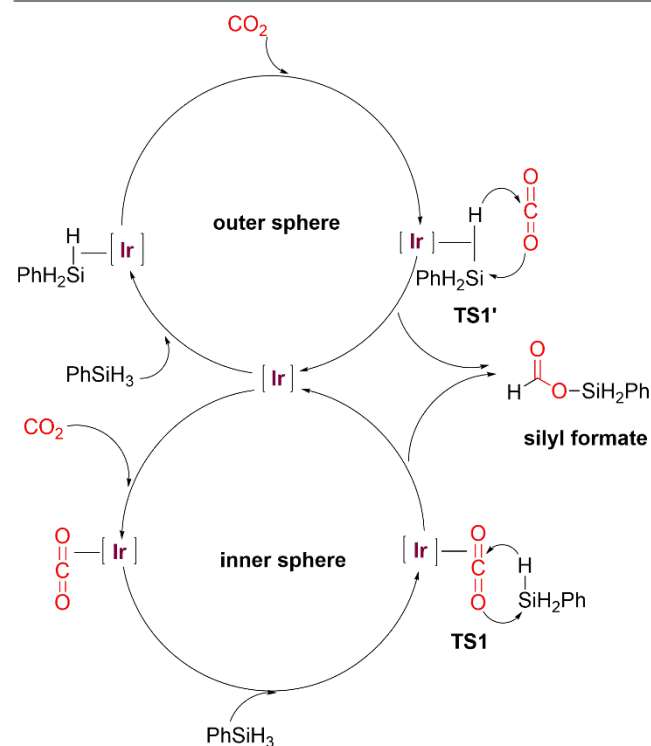


Figure 7. The possible reaction mechanism of CO₂ hydrosilylation.

To elucidate the reaction pathway, the energy barriers of the transit states of these steps that control the speed of reaction as rate-determining processes are calculated. For each pathway, there might be one hydrogen transfer from PhSiH₃ to CO₂ (TS1

in inner sphere or TSI' in outer sphere). Moreover, to depict the synergistic catalysis of Au clusters and Ir-PCN-222, an Au₄ cluster in transit states near the hydrogen transferring process is modelled. The corresponding energy barriers ΔG_r are listed in Table S4, from which the inner sphere pathway ($\Delta G_r = 118.50$ kJ·mol⁻¹) is expected to be more beneficial than the outer sphere pathway ($\Delta G_r = 123.71$ kJ·mol⁻¹). Nevertheless, the outer sphere pathway may not be completely ruled out due to the small energy difference.

4. CONCLUSION

In conclusion, a porphyrin metal-organic framework (PMOF) composite, Au@Ir-PCN-222, is found to be an effective catalyst for CO₂ hydrosilylation under mild conditions (R. T. and 1 atm), which might benefit from the synergistic catalysis of Ir-porphyrin units and Au NPs. Theoretical studies disclose the CO₂ molecules can be stored in the micro channels of Ir-PCN-222, and then diffuse to the meso channels where the catalytic reactions occur. Our work provides a useful strategy to integrate multiple functional components into MOFs for the combinatorial CO₂ adsorption and activation. Further work about the design and catalytic applications of PMOFs is on the process.

ASSOCIATED CONTENT

Supporting Information. Physical characterizations of catalysts, CO₂ adsorption and diffusion, catalysis and reaction mechanism, and characteriations of formamides. This material is available free of charge via the Internet at <http://pubs.acs.org>.

AUTHOR INFORMATION

Corresponding Author

zhli99@mail.sysu.edu.cn;
cesscy@mail.sysu.edu.cn

Author Contributions

+These authors contributed equally.

Notes

The authors declare no competing financial interest.

ACKNOWLEDGMENT

The authors acknowledge support from the National Natural Science Foundation of China (21773314, 21720102007, 21821003, and 21890380), the Guangdong Natural Science Funds for Distinguished Young Scholar (2019B151502017), the Tip-top Youth Talents of Guangdong special support program (No. 20173100042150021), Science and Technology Planning Project of Guangzhou (201707010168), the General Financial Grant from the China Postdoctoral Science Foundation (2019M662809), and Local Innovative and Research Teams Project of Guangdong Pearl River Talents Program (2017BT01C161).

REFERENCES

(1) Ding, M.; Flaig, R. W.; Jiang, H.-L.; Yaghi, O. M. Carbon capture and conversion using metal-organic frameworks and MOF-based materials. *Chem. Soc. Rev.* **2019**, *48*, 2783–2828.
(2) González-Sebastián, F. J.; Aitani, A. M.; Oro, L. A. Homogeneous catalytic reduction of CO₂ with hydrosilanes. *Catal. Sci. Technol.* **2014**, *4*, 611–624.

(3) Aresta, M.; Dibenedetto, A.; Quaranta, E. State of the art and perspectives in catalytic processes for CO₂ conversion into chemicals and fuels: The distinctive contribution of chemical catalysis and Biotechnology. *J. Catal.* **2016**, *343*, 2–45.
(4) Chen, J.; McGraw, M.; Chen, E. Y.-X. Diverse catalytic systems and mechanistic pathways for hydrosilylative reduction of CO₂. *ChemSusChem* **2019**, *12*, 4543–4569.
(5) González-Sebastián, L.; Flores-Alamo, M.; García, J. J. Nickel-Catalyzed Hydrosilylation of CO₂ in the Presence of Et₃B for the Synthesis of Formic Acid and Related Formates. *Organometallics* **2013**, *32*, 7186–7194.
(6) Fan, T.; Sheong, F. K.; Lin, Z. DFT Studies on Copper-Catalyzed Hydrocarboxylation of Alkynes Using CO₂ and Hydrosilanes. *Organometallics* **2013**, *32*, 5224–5230.
(7) Liu, X.-F.; Li, X.-Y.; He, L.-N. Transition Metal-Catalyzed Reductive Functionalization of CO₂. *Eur. J. Org. Chem.* **2019**, 2437–2447.
(8) Park, S.; Bézier, D.; Brookhart, M. An efficient iridium catalyst for reduction of carbon dioxide to methane with trialkylsilanes. *J. Am. Chem. Soc.* **2012**, *134*, 11404–11407.
(9) Matsuo, T.; Kawaguchi, H. From carbon dioxide to methane: Homogeneous reduction of carbon dioxide with hydrosilanes catalyzed by zirconium-borane complexes. *J. Am. Chem. Soc.* **2006**, *128*, 12362–12363.
(10) Steinhoff, P.; Paul, M.; Schroers, J. P.; Tauchert, M. E. Highly efficient palladium-catalysed carbon dioxide hydrosilylation employing PMP ligands. *Dalton Trans.* **2019**, *48*, 1017–1022.
(11) Frogneux, X.; Jacquet, O.; Cantat, T. Iron-catalyzed hydrosilylation of CO₂: CO₂ conversion to formamides and methylamines. *Catal. Sci. Technol.* **2014**, *4*, 1529–1533.
(12) Huang, Z.; Jiang, X.; Zhou, S.; Yang, P.; Du, C.-X.; Li, Y. Mn-catalyzed selective double and mono-N-Formylation and N-Methylation of amines by using CO₂. *ChemSusChem* **2019**, *12*, 3054–3059
(13) Tüchler, M.; Gärtner, L.; Fischer, S.; Boese, A. D.; Belaj, F.; Möscher-Zanetti, N. C. Efficient CO₂ insertion and reduction catalyzed by a terminal zinc hydride complex. *Angew. Chem. Int. Ed.* **2018**, *57*, 6906–6909.
(14) Jacquet, O.; Das Neves Gomes, C.; Ephritikhine, M.; Cantat, T. Recycling of carbon and silicon wastes: Room temperature formylation of N-H bonds using carbon dioxide and polymethylhydrosiloxane. *J. Am. Chem. Soc.* **2012**, *134*, 2934–2937.
(15) Zhou, Q.; Li, Y. The real role of N-heterocyclic carbene in reductive functionalization of CO₂: An alternative understanding from density functional theory study. *J. Am. Chem. Soc.* **2015**, *137*, 10182–10189.
(16) Chong, C. C.; Kinjo, R. Hydrophosphination of CO₂ and subsequent formate transfer in the 1,3,2-diazaphospholene-catalyzed N-formylation of amines. *Angew. Chem. Int. Ed.* **2015**, *54*, 12116–12120.
(17) Hota, P. K.; Sau, S. C.; Mandal, S. K. Metal-free catalytic formylation of amides using CO₂ under ambient conditions. *ACS Catal.* **2018**, *8*, 11999–12003.
(18) Zhang, X.; Sun, J.; Wei, G.; Liu, Z.; Yang, H.; Wang, K.; Fei, H. In situ generation of an N-heterocyclic carbene functionalized metal-organic framework by postsynthetic ligand exchange: efficient and selective hydrosilylation of CO₂. *Angew. Chem.* **2019**, *131*, 2870–2875.
(19) Zhang, X.; Jiang, Y.; Fei, H. UiO-type metal-organic frameworks with NHC or metal-NHC functionalities for N-methylation using CO₂ as the carbon source. *Chem. Commun.* **2019**, *55*, 11928–11931.
(20) Zhu, N.-X.; Wei, Z.-W.; Chen, C.-X.; Wang, D.; Cao, C.-C.; Qiu, Q.-F.; Jiang, J.-J.; Wang, H.-P.; Su, C.-Y. Self-generation of surface roughness by low-surface-energy alkyl chains for highly stable superhydrophobic/superoleophilic MOFs with multiple functionalities. *Angew. Chem. Int. Ed.* **2019**, *58*, 17033–17040.
(21) Cao, C.-C.; Chen, C.-X.; Wei, Z.-W.; Qiu, Q.-F.; Zhu, N.-X.; Xiong, Y.-Y.; Jiang, J.-J.; Wang, D.; Su, C.-Y. Catalysis through Dynamic Spacer Installation of Multivariate Functionalities in Metal-Organic Frameworks. *J. Am. Chem. Soc.* **2019**, *141*, 2589–2593.
(22) Luo, Y.-C.; Chu, K.-L.; Shi, J.-Y.; Wu, D.-J.; Wang, X.-D.; Mayor, M.; Su, C.-Y. Heterogenization of photochemical molecular devices:

- embedding a metal–organic cage into a ZIF-8-derived matrix to promote proton and electron transfer. *J. Am. Chem. Soc.* **2019**, *141*, 13057–13065.
- (23) Trickett, C. A.; Helal, A.; Al-Maythaly, B. A.; Yamani, Z. H. Cordova, K. E.; Yaghi, O. M. The chemistry of metal–organic frameworks for CO₂ capture, regeneration and conversion. *Nat. Rev. Mater.* **2017**, *2*, 17045.
- (24) Li, G.; Zhao, S.; Zhang, Y.; Tang, Z. Metal–Organic Frameworks Encapsulating Active Nanoparticles as Emerging Composites for Catalysis: Recent Progress and Perspectives. *Adv. Mater.* **2018**, 1800702.
- (25) Liu, X.; Sun, L.; Deng, W.-Q. Theoretical investigation of CO₂ adsorption and dissociation on low index surfaces of transition metals. *J. Phys. Chem. C* **2018**, *122*, 8306–8314.
- (26) Hou, S.-J.; Dong, J.; Zhao, B. Formation of C-X Bonds in CO₂ chemical fixation catalyzed by metal–organic frameworks. *Adv. Mater.* **2019**, 1806163.
- (27) Liang, J.; Huang, Y.-B.; Cao, R. Metal–organic frameworks and porous organic polymers for sustainable fixation of carbon dioxide into cyclic carbonates. *Coord. Chem. Rev.* **2019**, *378*, 32–65.
- (28) Zhao, M.; Yuan, K.; Wang, Y.; Li, G.; Guo, J.; Gu, L.; Hu, W.; Zhao, H.; Tang, Z. Metal–organic frameworks as selectivity regulators for hydrogenation reactions. *Nature* **2016**, *539*, 76–80.
- (29) Rungtaweeworant, B.; Baek, J.; Araujo, J. R.; Archanjo, B. S.; Choi, K. M.; Yaghi, O. M.; Somorjai, G. A. Copper nanocrystals encapsulated in Zr-based metal–organic frameworks for highly selective CO₂ hydrogenation to methanol. *Nano Lett.* **2016**, *16*, 7645–7649.
- (30) Yoshimaru, S.; Sadakiyo, M.; Staykov, A.; Katoc, K.; Yamauchi, M. Modulation of the catalytic activity of Pt nanoparticles through charge-transfer interactions with metal–organic frameworks. *Chem. Commun.* **2017**, *53*, 6720–6723.
- (31) Kobayashi, H.; Taylor, J. M.; Mitsuka, Y.; Ogiwara, N.; Yamamoto, T.; Toriyama, T.; Matsumura, S.; Kitagawa, H. Charge transfer dependence on CO₂ hydrogenation activity to methanol in Cu nanoparticles covered with metal–organic framework systems. *Chem. Sci.* **2019**, *10*, 3289–3294.
- (32) Corey, J. Y. Reactions of Hydrosilanes with Transition Metal Complexes and Characterization of the Products. *Chem. Rev.* **2011**, *111*, 863–1071.
- (33) Chen, J.; McGraw, M.; Chen, E. Y.-X. Diverse catalytic systems and mechanistic pathways for hydrosilylative reduction of CO₂. *ChemSusChem* **2019**, *12*, 4543–4569.
- (34) Liu, J.; Chen, L.; Cui, H.; Zhang, J.; Zhang, L.; Su, C.-Y. Applications of metal–organic frameworks in heterogeneous supramolecular catalysis. *Chem. Soc. Rev.* **2014**, *43*, 6011–6061.
- (35) Zhang, L.; Liu, J.; Su, C.-Y. Application of metal–organic frameworks in CO₂ capture and conversion. Noncovalent interactions in catalysis. Catalysis Series No. 36. *The Royal Society of Chemistry* **2019**, 455–478.
- (36) Zhang, L.; Liu, J.; Su, C.-Y. Porphyrin metal–organic frameworks in heterogeneous supramolecular catalysis. Series on Chemistry, Energy and the Environment V7, *World Scientific Publishing Co Pte Ltd* **2020**, 225–265.
- (37) Liu, J.; Fan, Y.-Z.; Li, X.; Wei, Z.; Xu, Y.-W.; Zhang, L.; Su, C.-Y. A porous rhodium(III)-porphyrin metal–organic framework as an efficient and selective photocatalyst for CO₂ reduction. *Appl. Catal. B* **2018**, *231*, 173–181.
- (38) Liu, J.; Fan, Y.-Z.; Li, X.; Xu, Y.-W.; Zhang, L.; Su, C.-Y. Catalytic space engineering of porphyrin metal–organic frameworks for combined CO₂ capture and conversion at a low concentration. *ChemSusChem* **2018**, *11*, 2340–2347.
- (39) Wang, Y.; Cui, H.; Wei, Z.-W.; Wang, H.-P.; Zhang, L.; Su, C.-Y. Engineering catalytic coordination space in a chemically stable Ir-porphyrin MOF with a confinement effect inverting conventional Si–H insertion chemoselectivity. *Chem. Sci.* **2017**, *8*, 775–780.
- (40) Li, S.; Mei, H.-M.; Yao, S.-L.; Chen, Z.-Y.; Lu, Y.-L.; Zhang, L.; Su, C.-Y. Well-distributed Pt-nanoparticles within confined coordination interspaces of self-sensitized porphyrin metal–organic frameworks: synergistic effect boosting highly efficient photocatalytic hydrogen evolution reaction. *Chem. Sci.* **2019**, *10*, 10577–10585.
- (41) Liu, G.; Cui, H.; Wang, S.; Zhang, L.; Su, C.-Y. A series of highly stable porphyrinic metal–organic frameworks based on iron-oxo chain cluster: design, synthesis and biomimetic catalysis. *J. Mater. Chem. A* **2020**, *8*, 8376–8382.
- (42) Feng, D.; Gu, Z.-Y.; Li, J.-R.; Jiang, H.-L.; Wei, Z.; Zhou, H.-C. Zirconium-metalloporphyrin PCN-222: mesoporous metal–organic frameworks with ultrahigh stability as biomimetic catalysts. *Angew. Chem. Int. Ed.* **2012**, *51*, 10307–10310.
- (43) Morris, W.; Voloskiy, B.; Demir, S.; Gándara, F.; McGrier, P. L.; Furukawa, H.; Cascio, D.; Stoddart, J. F.; Yaghi, O. M. Synthesis, structure, and metalation of two new highly porous zirconium metal–organic frameworks. *Inorg. Chem.* **2012**, *51*, 6443–6445.
- (44) Chen, Y.; Hoang, T.; Ma, S. Biomimetic catalysis of a porous iron-based metal–metalloporphyrin framework. *Inorg. Chem.* **2012**, *51*, 12600–12602.
- (45) Voloskiy, B.; Niwa, K.; Chen, Y.; Zhao, Z.; Weiss, N. O.; Zhong, X.; Ding, M.; Lee, C.; Huang, Y.; Duan, X. Metal-organic framework templated synthesis of ultrathin, well-aligned metallic nanowires. *ACS Nano* **2015**, *9*, 3044–3049.
- (46) Chen, Y.-Z.; Jiang, H.-L. Porphyrinic metal–organic framework catalyzed heck-reaction: Fluorescence “turn-on” sensing of Cu(II) ion. *Chem. Mater.* **2016**, *28*, 6698–6704.
- (47) Wang, Q.; Xu, R.; Wang, X.-S.; Liu, S.-D.; Huang, Y.-B.; Cao, R. Platinum nanoparticle-decorated porous porphyrin-based metal–organic framework for photocatalytic hydrogen production. *Chinese J. Inorg. Chem.* **2017**, *33*, 2038–2044.
- (48) Hutter, J.; Lannuzzi, M.; Sciffmann, F.; VandeVondele, J. CP2K: atomistic simulations of condensed matter systems. *Wiley Interdiscip. Rev. Comput. Mol. Sci.* **2014**, *4*, 15–25.
- (49) Perdew, J. P.; Burke, K.; Ernzerhof, M. Generalized gradient approximation made simple. *Phys. Rev. Lett.* **1996**, *77*, 3865–3868.
- (50) Joost, V.; Hutter, J. Gaussian basis sets for accurate calculations on molecular systems in gas and condensed phases. *J. Chem. Phys.* **2007**, *127*, 114105.
- (51) Goedecker, S.; Teter, M.; Hutter, J. Separable dual-space Gaussian pseudopotentials. *Phys. Rev. B* **1996**, *54*, 1703–1710.
- (52) Frisch, M. J.; Trucks, G. W.; Schlegel, H. B.; Scuseria, G. E.; Robb, M. A.; Cheeseman, J. R.; Scalmani, G.; Barone, V.; Mennucci, B.; Petersson, G. A.; Nakatsuji, H.; Caricato, M.; Li, X.; Hratchian, H. P.; Izmaylov, A. F.; Bloino, J.; Zheng, G.; Sonnenberg, J. L.; Hada, M.; Ehara, M.; Toyota, K.; Fukuda, R.; Hasegawa, J.; Ishida, M.; Nakajima, T.; Honda, Y.; Kitao, O.; Nakai, H.; Vreven, T.; Montgomery, J. A. J.; Peralta, J. E.; Ogliaro, F.; Bearpark, M.; Heyd, J. J.; Brothers, E.; Kudin, K. N.; Staroverov, V. N.; Keith, T.; Kobayashi, R.; Normand, J.; Raghavachari, K.; Rendell, A.; Burant, J. C.; Iyengar, S. S.; Tomasi, J.; Cossi, M.; Rega, N.; Millam, J. M.; Klene, M.; Knox, J. E.; Cross, J. B.; Bakken, V.; Adamo, C.; Jaramillo, J.; Gomperts, R.; Stratmann, R. E.; Yazyev, O.; Austin, A. J.; Cammi, R.; Pomelli, C.; Ochterski, J. W.; Martin, R. L.; Morokuma, K.; Zakrzewski, V. G.; Voth, G. A.; Salvador, P.; Dannenberg, J. J.; Dapprich, S.; Daniels, A. D.; Farkas, O.; Foresman, J. B.; Ortiz, J. V.; Cioslowski, J.; Fox, D. J., *Gaussian 09, Revision D.01*; Gaussian, Inc.: Wallingford, CT, 2013.
- (53) Breneman, C. M.; Wiberg, K. B. Determining atom-centered monopoles from molecular electrostatic potentials—the need for high sampling density in formamide conformational-analysis. *J. Comput. Chem.* **1990**, *11*, 361–73.
- (54) Zhao, Y.; Truhlar, D. G.; A new local density functional for main-group thermochemistry, transition metal bonding, thermochemical kinetics, and noncovalent interactions, *J. Chem. Phys.* **2006**, *125*, 1–18.
- (55) Binning, R. C.; Curtiss, L. A. Compact contracted basis-sets for 3rd-row atoms -GA-KR, *J. Comput. Chem.* **1990**, *11*, 1206–16.
- (56) Wedig, U.; Dolg, M.; Stoll, H.; Preuss, H. Quantum chemistry: the challenge of transition metals and coordination chemistry[M]. Springer, Dordrecht, **1986**, 79–89.
- (57) Batsanov, S. Van der Waals radii of elements. *Inorg. Mater.* **2001**, *37*, 871–885.
- (58) Garzón, I. L.; Michaelian, K.; Beltrán, M. R.; Posada-Amarillas, A.; Ordejón, P.; Artacho, E.; Sánchez-Portal, D.; Soler, J. M. Lowest energy structures of gold nanoclusters. *Phys. Rev. Lett.* **1998**, *81*, 1600–1603.

- (59) Zhang, Y.; Yang, W. Comment on "Generalized gradient approximation made simple". *Phys. Rev. Lett.* **1998**, *80*, 890.
- (60) Rappé, A. K.; Casewit, C. J.; Colwell, K. S.; Goddard III, W. A.; Skiff, W. M. UFF, a full periodic table force field for molecular mechanics and molecular dynamics simulations. *J. Am. Chem. Soc.* **1992**, *114*, 10024–10035.
- (61) Mayo, S. L.; Olafson, B. D.; Goddard, W. A. DREIDING: a generic force field for molecular simulations. *J. Phys. Chem.* **1990**, *94*, 8897–8909.
- (62) Harris, J. G.; Yung, K. H. Carbon dioxide's liquid-vapor coexistence curve and critical properties as predicted by a simple molecular model. *J. Phys. Chem.* **1995**, *99*, 12021–12024.
- (63) Peng, D.-Y.; Robinson, D. B.; A new two-constant equation of state. *Ind. Eng. Chem. Res.* **1976**, *15*, 59–64.
- (64) Yang, Q.; Zhong, C. Molecular simulation of carbon dioxide / methane / hydrogen mixture adsorption in metal-organic frameworks. *J. Phys. Chem. B.* **2006**, *110*, 17776–17783.
- (65) Vlugt, T. J. H.; Garcia-Perez, E.; Dubbeldam, D.; Ban, S.; Calero, S. Computing the heat of adsorption using molecular simulations: the effect of strong Coulombic interactions. *J. Chem. Theo. Comput.* **2008**, *4*, 1107–1118.
- (66) <http://lammps.sandia.gov>.
- (67) Schneider T.; Stoll E. Molecular-dynamics study of a three-dimensional one-component model for distortive phase transitions. *Phys. Rev. B.* **1978**, *17*, 1302–1322.
- (68) Kantorovich, L. Generalized Langevin equation for solids. I. Rigorous derivation and main properties. *Phys. Rev. B.* **2008**, *78*, 094304.
- (69) Myshakin, E. M.; Saidi, W. A.; Romanov, V. N. Cygan, R. T.; Jordan, K. D. J. Molecular dynamics simulations of carbon dioxide intercalation in hydrated Na-montmorillonite. *Phys. Chem. C* **2013**, *117*, 21, 11028-11039.
- (70) Skoulidas, A. I.; Sholl, D. S. Transport diffusivities of CH₄, CF₄, He, Ne, Ar, Xe, and SF₆ in silicalite from atomistic simulations. *J. Phys. Chem. B.* **2002**, *106*, 5058–5067.
- (71) Weigend, F.; Ahlrichs, R. Balanced basis sets of split valence, triple zeta valence and quadruple zeta valence quality for H to Rn: Design and assessment of accuracy. *Phys. Chem. Chem. Phys.* **2005**, *7*, 3297–3305.
- (72) Weigend, F. Accurate Coulomb-fitting basis sets for H to Rn. *Phys. Chem. Chem. Phys.* **2006**, *8*, 1057–1065.
- (73) Lu, X.; Rycenga, M.; Skrabalak, S. E.; Wiley, B.; Xia, Y. Chemical synthesis of novel plasmonic nanoparticles. *Annu. Rev. Phys. Chem.* **2009**, *60*, 167–92.
- (74) Řezáč J., Hobza P. Advanced corrections of hydrogen bonding and dispersion for semiempirical quantum mechanical methods. *J. Chem. Theo. Comput.* **2012**, *8*, 141–151.
- (75) Plant, D.; Jobic, H.; Llewellyn, P.; Maurin, G. Diffusion of CO₂ in NaY and NaX faujasite systems: quasi-elastic neutron scattering experiments and molecular dynamics simulations. *Eur. Phys. J. Spec. Top.* **2007**, *141*, 127–132.
- (76) Yang, Q.; Jobic, H.; Salles, F.; Kolokolov, D.; Guillerm, V.; Serre, C.; Maurin, G. Probing the Dynamics of CO₂ and CH₄ within the Porous Zirconium Terephthalate UiO-66(Zr): A Synergic Combination of Neutron Scattering Measurements and Molecular Simulations. *Chem.-Eur. J.* **2011**, *17*, 8882–8889.
- (77) Wang, S.-G.; Liao, X.-Y.; Cao, D.-B.; Huo, C.-F.; Li, Y.-W.; Wang, J.; Jiao, H. Factors controlling the interaction of CO₂ with transition metal surfaces. *J. Phys. Chem. C* **2007**, *111*, 16934–16940.

TOC

